JOURNAL OF SYNCHROTRON RADIATION

ISSN 1600-5775

Received 21 April 2020
Accepted 7 May 2020

Edited by I. Lindau, SLAC/Stanford University, USA

Keywords: hafnia–silicate–zirconate nanostructure; sol-gel method; spectroscopy; XANES; EXAFS.; composites; sol-gel; XAS.

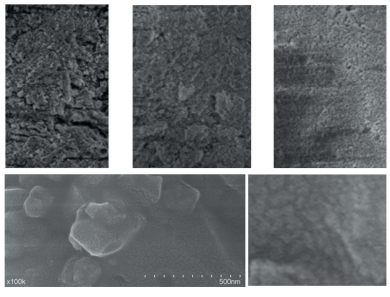

Characteristics and local structure of hafnia-silicate-zirconate ceramic nanomixtures

L. Pop,[a] S. Rada,[a,b]* P. An,[c] J. Zhang,[c] M. Rada,[b] R. C. Suciu[b] and E. Culea[a]

[a]Department of Physics and Chemistry, Technical University of Cluj-Napoca, Cluj-Napoca 400020, Romania, [b]National Institute for Research and Development of Isotopic and Molecular Technologies, Cluj-Napoca 400293, Romania, and [c]Institute of High Energy Physics, Chinese Academy of Sciences, Beijing 100049, People's Republic of China. *Correspondence e-mail: simona.rada@phys.utcluj.ro

Zirconate systems having the composition $3HfO_2{\cdot}15SiO_2{\cdot}xY_2O_3{\cdot}(82-x)ZrO_2$, where x = 2, 7 and 12 mol% Y_2O_3, were synthesized by a sol-gel method. The analysis of X-ray diffraction data showed the presence of the t-ZrO_2, m-ZrO_2, m-HfO_2, Y_2SiO_5 and $Y_2Si_2O_7$ crystalline phases in a ceramic nanomixture. Spectroscopic data show that the increase of the Y_2O_3 content of samples determines the increase of the t-ZrO_2, m-HfO_2 and silicate crystalline phases. Gap energy values decrease almost linearly with increasing Y_2O_3 content of samples. A detailed study of XANES data does not show a significant difference with increasing Y_2O_3 content of the samples suggesting an appreciable stability of the hafnium ions +4 oxidation state and their microvicinity. EXAFS results show that the local structure around the Hf cation is similar to that from the monoclinic crystalline HfO_2 where the Hf–O coordination number tends to 7. The bond lengths of Hf–O shells show small deviations from ~2.12 Å and the Hf–metal paths become more structured by increasing the Y_2O_3 content of the samples.

1. Introduction

Zirconium oxide based systems have been drawing increasing attention of researchers due to their unique properties that are promising for biomedical applications. Thus, ceramics based on ZrO_2 are well known for their low thermal conductivity, high fracture toughness and biocompatibility in comparison with other materials (Ponnilavan *et al.*, 2015).

As has been observed up to now, pure zirconia (ZrO_2) possesses three polymorph structures: cubic (c-ZrO_2), tetragonal (t-ZrO_2) and monoclinic (m-ZrO_2). The t-ZrO_2 and m-ZrO_2 phase transformation has important technological consequences, since the extensive microcracking caused by the anisotropic volume expansion accompanying the reaction leads to the loss of mechanical integrity in sintered bodies. When a metal oxide with a lower valence cation is incorporated into cubic ZrO_2, the fluorite-type cubic phase is stabilized. One of the common 'stabilizers' is yttrium oxide since it has good physical and chemical stability (Torres & Llopis, 2009; Qin *et al.*, 2012; Singh *et al.*, 2015). The substitution of this lower valence cation (+3) in the Zr^{+4} sublattice sites creates oxygen vacancies. The Y_2O_3 can stabilize the fluorite-type cubic structure and hence avoid the problem of the t-ZrO_2 and m-ZrO_2 transformation by eliminating the t-phase (Wu *et al.*, 1992; Chu *et al.*, 2016).

Further, the dual role of zirconia in glass matrices was confirmed as a network former and/or as a network modifier. Thus, zirconia playing the network former role leads to a network consisting of ZrO_4 tetrahedra while playing the

network modifier role leads to a network consisting of ZrO_6 octahedra with four bridging and two non-bridging oxygen atoms (Glazneva *et al.*, 2012). Addition of HfO_2 to ZrO_2 enhances the chemical stability and thermal-shock resistance of the host ceramic (Zhen *et al.*, 2007; Karunarathne *et al.*, 2017). Note that zirconia containing silicon oxide has attracted attention too because of its excellent resistance to alkali corrosion and its low thermal expansion (Simhan, 1983; Kwon *et al.*, 2017). In such a material, hafnium oxide or zirconium oxide were the best metal oxides to replace the silicon dioxide.

Note that fundamental studies on the crystalline structure and microstructure of monoclinic ZrO_2 ceramics with or without dopants have rarely been reported (Kwon *et al.*, 2017; Rada, Culea *et al.*, 2018). The research on monoclinic ZrO_2 ceramics can be associated with difficulties in the manufacturing process and the mechanical instability at temperature variations.

The ZrO_2–Y_2O_3 compositions are candidates for the transmutation of radionuclides in reactors and as accelerator-based neutron sources due to their high radiation resistance (Moll *et al.*, 2009).

Taking into account the important properties of the oxides presented above, we prepared some new ceramics containing all of these oxides using the sol-gel method. Considering the development of new materials with mixed compositions, the experimental conditions can be adjusted in order to obtain stable or metastable compounds. The physical and chemical properties of mixed oxides prepared by the sol-gel method are of great interest due to their thermal and chemical properties and because they are highly acidic due to the presence of OH groups on the surface.

Bearing in mind the above-mentioned aspects, in this study we wanted to prepare some new zirconate materials with potential biomedical and optical applications. Thus, new zirconate nanostructures were prepared in the $3HfO_2{\cdot}15SiO_2{\cdot}xY_2O_3{\cdot}(82-x)ZrO_2$ system where x = 2, 7 and 12 mol% Y_2O_3 via the sol-gel method. To the best of our knowledge, this system has not been reported in the scientific literature until now.

The investigation of the $3HfO_2{\cdot}15SiO_2{\cdot}xY_2O_3{\cdot}(82-x)ZrO_2$ zirconate materials was carried out by X-ray diffraction (XRD) and scanning electron microscope (SEM) analysis, Fourier transform infrared (FT-IR), UV-Vis, photoluminescence (PL), Raman and X-ray absorption spectroscopies. X-ray absorption spectroscopy (XAS) with its two amendments, X-ray absorption near-edge structure (XANES) and extended X-ray absorption fine structure (EXAFS), represents an important investigation technique of the local structure around ions of interest. Thus, EXAFS analysis was used to study the structure of the Hf atoms' microvicinity, their coordination number and the length of the bonds involving Hf atoms.

First, one of the main objectives of the present work was to perform the structural characterization of the studied new zirconate materials. Our interest was focused on obtaining structural information (via XRD, SEM analysis, FTIR and X-ray absorption spectroscopies) concerning the characteristic crystalline phases and structural units that occur in the studied materials. Second, some spectroscopic properties of the studied zirconate samples were investigated (by using FT-IR, UV-Vis, PL and Raman spectroscopies) to find out their potential applications for optical devices. The electronic transitions that take place were studied. Finally, the influence of the addition of Y_2O_3 was followed, since dopants can be useful tools to improve the structural and/or behavioral properties of the host materials.

2. Experimental data

Tetraethoxysilane and high purity ZrO_2, Y_2O_3 and HfO_2 powders were used as starting materials. Tetraethoxysilane was diluted with ethanol. Solutions of $Zr(NO_3)_4$, $Y(NO_3)_3$ and $Hf(NO_3)_4$ were prepared by dissolving ZrO_2, Y_2O_3 and HfO_2 into HNO_3 solutions of pH = 2. Suitable volumes of tetraethoxysilane, $Zr(NO_3)_4$, $Y(NO_3)_3$ and $Hf(NO_3)_4$ were mixed and stirred at 70°C to obtain homogeneous solutions. The resulting solutions were stirred at 100°C until a dry powder was obtained after the evaporation of H_2O. These dried powders were uniaxially compacted under pressure in the form of disks (2 mm thick, 9 mm diameter). The disks were calcined in alumina crucibles using an electric furnace heated at 1400°C for two hours. The disks were put into the electric furnace direct at this temperature. After two hours, the melted disk materials were quenched at room temperature by pouring onto a stainless-steel plate.

The samples were characterized by several methods: XRD, SEM analysis, FTIR, UV-Vis, PL, Raman and XAS spectroscopy that were previously described by Rada *et al.* (2013, 2017, 2019), Rada, Zhang *et al.* (2018) and Dehelean *et al.* (2016).

The changes of the microstructure of the samples by doping were characterized by analysing the profile of the diffraction peaks and SEM micrographs. FTIR spectroscopy was recorded to determine the presence of the specific structural units, such as zirconia or silicate network in the prepared samples. UV-Vis data were used to determine the gap energy. The UV-Vis, PL and Raman spectroscopy were also used to show the presence of the zirconia polymorphs. The XRD peaks of monoclinic zirconia and monoclinic hafnia are very similar because they arise at nearly the same angles. XANES and EXAFS were performed in order to indicate the formation of the HfO_2 crystalline phase with monoclinic structure.

3. Results and discussion

3.1. XRD data

X-ray diffraction was used to identify the main crystalline phases in the studied samples. Fig. 1 shows the XRD patterns of the samples from the $3HfO_2{\cdot}15SiO_2{\cdot}xY_2O_3{\cdot}(82-x)ZrO_2$ system where x = 2, 7 and 12 mol% Y_2O_3. All diffractograms show peaks characteristic of crystalline phases. In order to identify the crystalline phases that appear in the diffraction

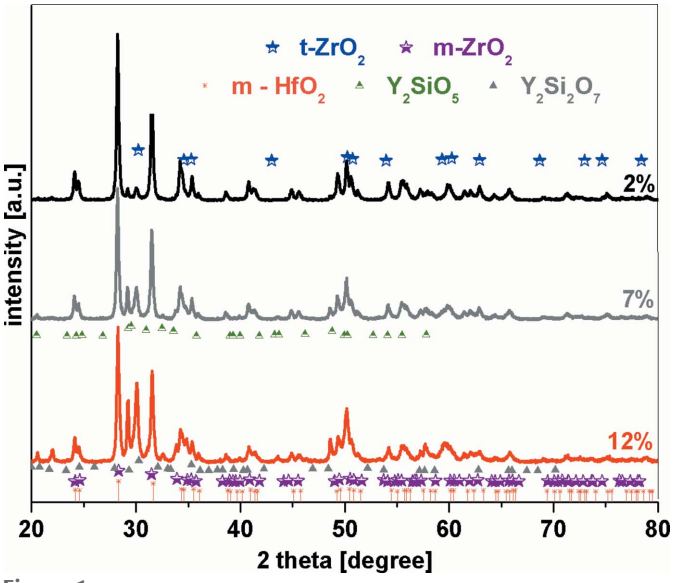

Figure 1
X-ray diffraction patterns for the $3HfO_2{\cdot}15SiO_2{\cdot}xY_2O_3{\cdot}(82 - x)ZrO_2$ system.

patterns we followed a standard procedure, namely computer analysis based on the powder diffraction file (PDF).

This analysis permitted the identification of five crystalline phases present in the samples. Two of these phases belong to the ZrO_2 crystalline phase with monoclinic (PDF No. 03-065-1024, monoclinic lattice with a = 5.14608 Å, b = 5.21177 Å, c = 5.31302 Å and α = 99.222° cell parameter) and tetragonal (PDF No. 00-050-1089, a = 3.5984 Å, c = 5.152 Å) symmetry. The HfO_2 crystalline phase with monoclinic structure (PDF No. 00-034-0104, monoclinic lattice with a = 5.2851, b = 5.1819, c = 5.1157 Å cell parameter), the yttrium silicate (Y_2SiO_5, PDF No. 00-021-1456) and yttrium disilicate ($Y_2Si_2O_7$, PDF No. 00-021-1459) crystalline phases were also shown in the studied samples. The assignments of the most important crystalline peaks are shown in Fig. 1. The X-ray diffractograms from Fig. 1 show that by increasing the yttrium content of samples, x, the relative intensity of the peaks attributed to the monoclinic ZrO_2 decreases, while the relative intensity of peaks assigned to the tetragonal ZrO_2 phase increase. Bearing in mind different potential applications, this is an important evolution since the tetragonal ZrO_2 is more stable that the monoclinic one.

The ($\bar{1}$11) and (111) reflection peaks situated at about 28.2° and 31.4° of the monoclinic ZrO_2 crystalline phase (Rada, Culea *et al.*, 2018) did not appear to be significantly modified by increasing the Y_2O_3 content of the samples. Analysis of the reflections in the XRD patterns of the monoclinic ZrO_2 phase and monoclinic HfO_2 crystalline phase shows the same satellite peaks. Accordingly, it is difficult to follow the effect of the Y_2O_3 content on the amount of monoclinic ZrO_2 phase in the studied samples.

A small amount of $Y_2Si_2O_5$ crystalline phase was detected in the sample with x = 2 mol% Y_2O_3. By increasing the Y_2O_3 content up to x = 7 mol%, the intensity of the characteristic peaks of the Y_2SiO_5 crystalline phase increases. After that, at a higher Y_2O_3 content, x = 12 mol%, a new diffraction peak centered at about 22.03° can be seen suggesting the presence of the $Y_2Si_2O_7$ crystalline phase. This compositional evolution shows that by increasing the yttrium ions content of samples the zirconia host matrix was converted into a yttrium–silicate–zirconia matrix. The excess of oxygen atoms can be accommodated in the host matrix by the formation of yttrium silicates.

3.2. FT-IR data

The FT-IR spectra of the $3HfO_2{\cdot}15SiO_2{\cdot}xY_2O_3{\cdot}(82 - x)ZrO_2$ samples with x = 2, 7 and 12 mol% are shown in Fig. 2. Each FT-IR absorption band is related to some vibration type specific of the structural groups that build up the investigated samples. The positions and assignments of the most important absorption bands shown in the FT-IR spectra are discussed. The assignments were made based on data from the literature concerning some vitreous or crystalline compounds related to the system investigated in this work (Lee & Condrate, 1988; Choi & Choy, 2016; Vitanov *et al.*, 2014; Ortiz *et al.*, 2005; Khomenkova *et al.*, 2014; Najafinezhad *et al.*, 2017; Ferdov *et al.*, 2012).

According to Lee & Condrate (1988), the wavenumber and/or intensity of vibrational modes involving Zr—O bonds will vary depending upon the arrangement of the oxygen atoms around the zirconium atoms. Thus, several zirconium–oxygen structural units can be considered with respect to the Zr—O stretching modes: ZrO_4 units, ZrO_6 units, monoclinic zirconia-type ZrO_7 units, tetragonal zirconia-type ZrO_8 units and cubic zirconia-type ZrO_8 units.

The absorption bands around 436, 386 and 310 cm^{-1} are present in all the studied samples (Fig. 2). These bands can be assigned to the symmetric and/or asymmetric stretching vibrations of chemical bonds in which zirconium and hafnium ions are involved.

The FT-IR features situated at about 525 cm^{-1}, 580 cm^{-1} and 745 cm^{-1} are due to Zr—O—Zr asymmetric and Zr—O

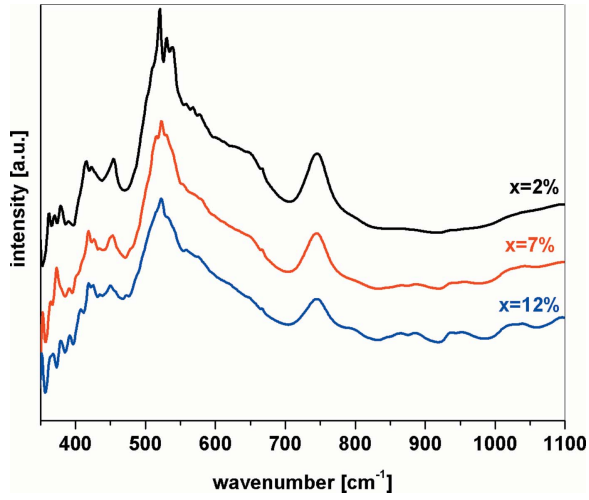

Figure 2
Infrared spectra of the $3HfO_2{\cdot}15SiO_2{\cdot}xY_2O_3{\cdot}(82 - x)ZrO_2$ system.

stretching modes and confirm the presence of monoclinic ZrO_2 phases in the studied system. The intensity of the mentioned vibrational features becomes less prominent with increasing the Y_2O_3 content of samples. In addition, a new weak IR feature associated with the Zr—O vibrations in tetragonal ZrO_2 crystalline structure appears around 600 cm^{-1} for x = 12 mol% Y_2O_3. Note that this crystalline phase was detected by XRD analysis, too.

The IR bands centered at about 870, 960 and 1020 cm^{-1} can be associated with the symmetric and antisymmetric stretching vibrations of the silicate units. By increasing the Y_2O_3 dopant level up to 12 mol%, the intensities of these bands increase, suggesting the formation of higher amounts of yttrium silicates in the host matrix.

The structural changes observed by the FT-IR investigation suggest that the yttrium ions play a network modifier role in the studied $3HfO_2{\cdot}15SiO_2{\cdot}xY_2O_3{\cdot}(82-x)ZrO_2$ system. These structural changes, determined by increasing the Y_2O_3 content of the samples, consist of the increase of the tetragonal ZrO_2 and silicate crystalline phases. This assumption is in good agreement with the results of the XRD investigation. The observed compositional evolution shows that the Y_2O_3 content can be used as an efficient tool to improve the stability of the studied system.

3.3. UV-Vis data

The UV-Vis spectra of the $3HfO_2{\cdot}15SiO_2{\cdot}xY_2O_3{\cdot}(82-x)ZrO_2$ zirconate nanostructures where x = 2, 7 and 12 mol% are given in Fig. 3. The samples show a very intense absorption in the UV region and a moderate absorption in the visible region. The bands from 225 nm, 265 nm and 350 nm correspond to the metal–ligand charge-transfer (oxygen electron from the free orbital of the metal ion). The absorption band from 225 nm is the highest one and is assigned to the charge transfers (i) from the oxygen anions to the zirconium cations ($O^{2-} \rightarrow Zr^{4+}$) in ZrO_2 and (ii) from the oxygen anions to the hafnium cations ($O^{2-} \rightarrow Hf^{4+}$) in HfO_2 (Fan *et al.*, 2017; Qi & Zhou, 2015).

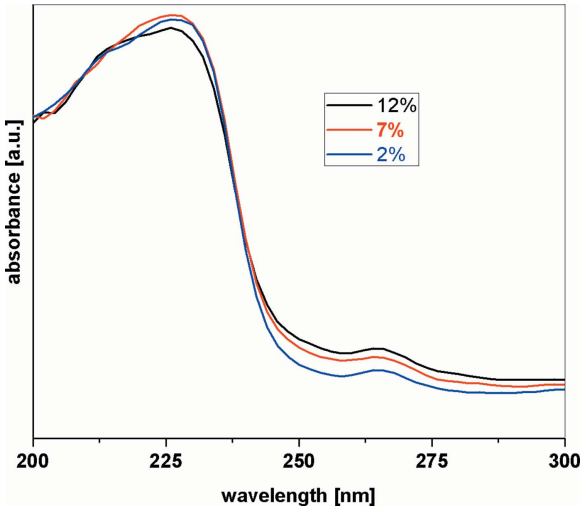

Figure 3
UV-Vis spectra of the $3HfO_2{\cdot}15SiO_2{\cdot}xY_2O_3{\cdot}(82-x)ZrO_2$ system.

The appearance of the UV absorption band centered at about 265 nm indicates the formation of tetragonal ZrO_2 phase (Balaji *et al.*, 2017). By increasing the Y_2O_3 content, the intensity of this band increases.

Villabona-Leal *et al.* (2014) consider that the UV-Vis absorption bands around 250 nm and 220 nm are due to different ZrO_2 crystalline phases, namely the monoclinic (the 250 nm band) and tetragonal (the 220 nm) ones.

The UV-Vis feature at 350 nm is intense for the lowest content of Y_2O_3, flattened for the middle content and then disappears at the maximum yttrium content. This evolution can be assigned to the structural changes that occur in the samples. Thus, according to the XRD and FT-IR data, it is possible to associate the compositional evolution of this feature with the increase of the tetragonal ZrO_2 crystalline phase and the decrease of the monoclinic ZrO_2 crystalline phase, respectively.

Using the UV-Vis spectra of the $3HfO_2{\cdot}15SiO_2{\cdot}xY_2O_3{\cdot}(82-x)ZrO_2$ system, we determined the gap energy of the samples. The calculated gap energy values are presented in Fig. 4. The values for the direct gap energy are between 4.87 eV and 5.05 eV, whereas those for the indirect gap energy are between 5.12 and 5.14 eV. Both direct and indirect gap energy values decrease almost linearly with increasing the Y_2O_3 content of the samples. Differences in the band gaps suggest different distributions and densities of the electronic states. The smaller values of the gap energy for the ceramic nanomixtures indicate smaller average crystallite sizes, in agreement with the SEM data.

3.4. PL spectra

Pure zirconium and hafnium oxide samples containing only monoclinic phases show broadband PL emissions situated at about 490 nm. The microscopic origin of these PL bands is still disputable (Kiisk *et al.*, 2016).

The PL spectra of the $3HfO_2{\cdot}15SiO_2{\cdot}xY_2O_3{\cdot}(82-x)ZrO_2$ samples with x = 2, 7 and 12 mol% Y_2O_3 are shown in Fig. 5. These spectra exhibit a broad band situated between 300 and 750 nm which is indicative of a white emission. This broad band consists of four PL bands of higher emission centered at about 335, 410, 450 and 470 nm and of two weak PL bands located at about 530 and 650 nm. The above-mentioned emission bands can be associated with structural defects such as oxygen vacancies in monoclinic ZrO_2 and monoclinic HfO_2 structures.

The high-intensity PL band located at about 410 nm and the bands centered at about 530 and 650 nm can be caused by interstitial defects such as oxygen vacancies in HfO_2 and ZrO_2 crystalline phases with monoclinic structure when Hf and Zr atoms are seven-coordinated. The O atoms can occupy the threefold and fourfold positions and the average Hf—O bond length is 2.08 and 2.20 Å, respectively (Chuang *et al.*, 2012). Therefore, the fourfold-coordinated O atom around the four adjacent Hf atoms is more susceptible to forming a vacancy.

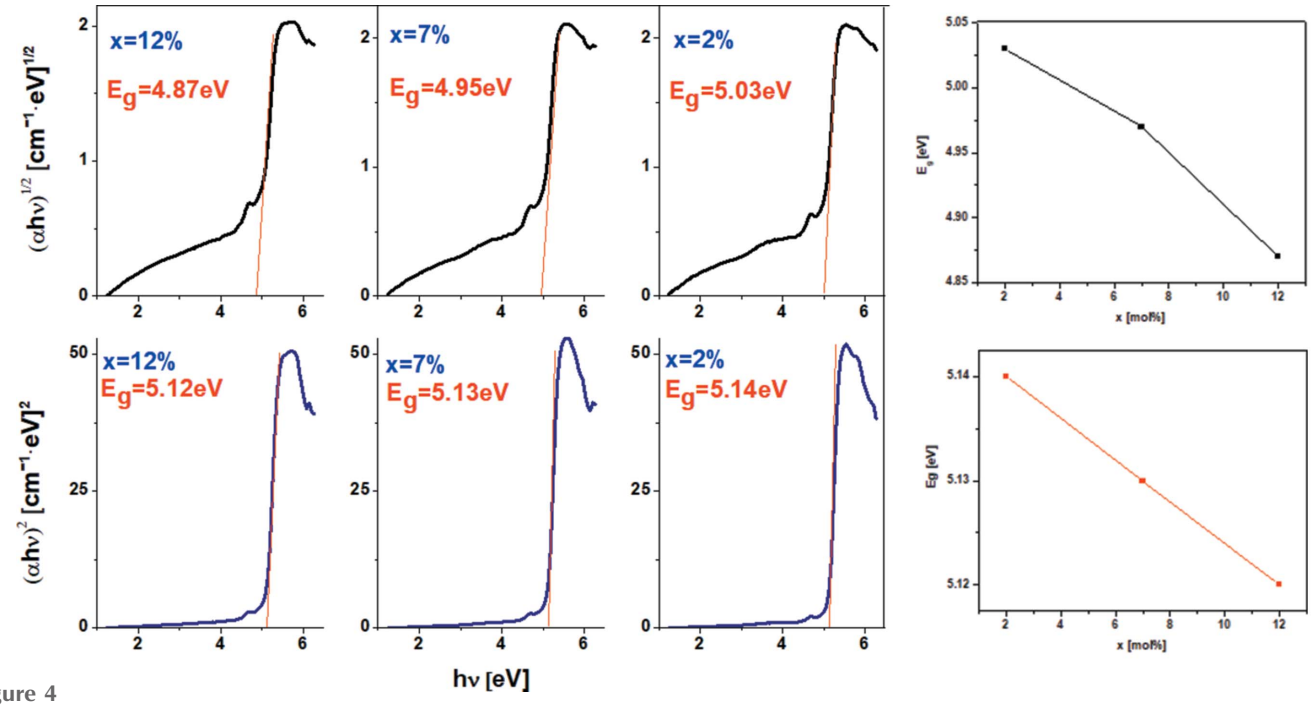

Figure 4
$(\alpha h\nu)^{1/2}$ and $(\alpha h\nu)^2$ as a function of photon energy for the $3HfO_2{\cdot}15SiO_2{\cdot}xY_2O_3{\cdot}(82-x)ZrO_2$ system; and the dependence of the optical band gap for the $3HfO_2{\cdot}15SiO_2{\cdot}xY_2O_3{\cdot}(82-x)ZrO_2$ system.

The stronger PL emission situated at ∼530 nm can be due to a fourfold-coordinated O atom in the HfO_2 structure.

As mentioned, the PL spectra of the $3HfO_2{\cdot}15SiO_2{\cdot}xY_2O_3{\cdot}(82-x)ZrO_2$ samples are related to structural oxygen vacancies. The intensity of the PL emission bands increases with increasing Y_2O_3 content of the samples. This behavior can be explained by considering that the small particle size was the main reason for the broad photoluminescence band.

3.5. XANES data

XANES measurements in fluorescence mode were performed using the X-ray energy of the incident flux in the range 9400–10400 eV. The L_3-edge of hafnium is located at about 9562 eV.

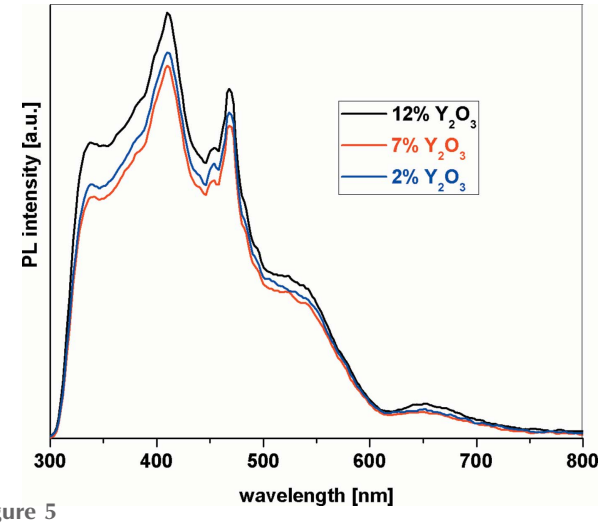

Figure 5
Photoluminescence spectra of the samples in the $3HfO_2{\cdot}15SiO_2{\cdot}xY_2O_3{\cdot}(82-x)ZrO_2$ composition where x = 2, 7 and 12 mol% Y_2O_3.

Zirconium and hafnium oxides are known to produce similar phase transitions under temperature and pressure variation. Under normal conditions of temperature and pressure, both oxides are in the monoclinic phase because the zirconium and hafnium cations have the same valence configuration with very similar ionic radii (0.78 Å for Zr^{+4} and 0.76 Å for Hf^{+4}). Since the crystallographic structures of the monoclinic phase of zirconium and hafnium are very close, many of the XRD peaks arise at nearly the same angles (Benyagoub, 2012). The transition temperature from the tetragonal to the monoclinic phase is higher in the case of HfO_2 (∼1700°C) than for ZrO_2 (∼1200°C). Note also that the Y^{+3} ions have radii (0.96 Å) larger than those of Zr^{+4} or Hf^{+4} ions and thus their insertion in the host matrix will produce lattice distortion and the elongation of the bonds with the oxygen ions.

Fig. 6 shows the XANES spectra for the Hf L_3-edge from 9525 to 9700 eV for the zirconate nanostructures in the $3HfO_2{\cdot}15SiO_2{\cdot}xY_2O_3{\cdot}(82-x)ZrO_2$ composition with x = 2, 7 and 12 mol% Y_2O_3. The second derivative Hf L_3-edge XANES spectra are also presented in the lower graph of Fig. 6 and permit the variation in the energy to be distinguished.

The XANES features at the Hf L_3-edge of the studied composites show a strong main peak centered at about 9562 eV (feature A) corresponding to the Hf^{+4} ions. In the post-edge region, a small peak located at about 9578 eV (feature B) and a broad peak situated around 9604 eV (feature C) were found.

The analysis of the XANES and second derivative spectra of the Hf L_3-edge indicates that the Y_2O_3 content of samples

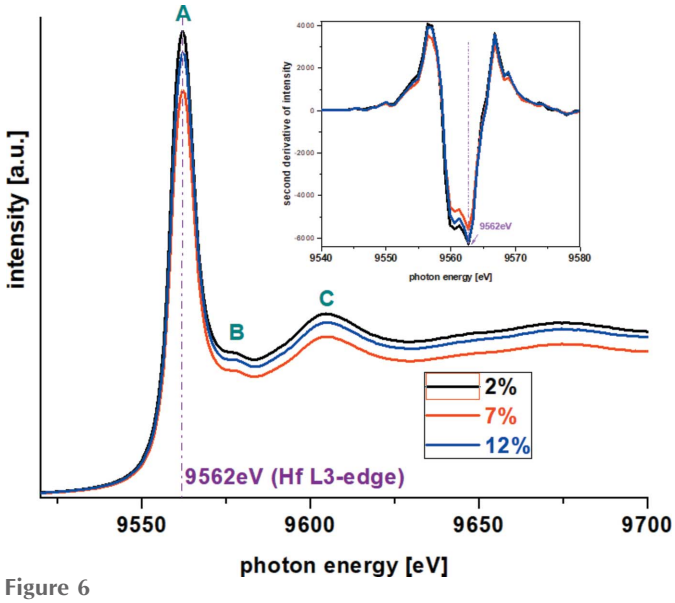

Figure 6
Hf L_3-edge XANES spectra of the studied samples in the $3HfO_2{\cdot}15SiO_2{\cdot}xY_2O_3{\cdot}(82-x)ZrO_2$ system where x = 2, 7 and 12 mol% Y_2O_3. The lower graph shows the second derivative Hf L_3-edge XANES spectra.

do not affect the edge position of the peaks that remains the same for all the studied ceramics but influences the peaks' intensity. Thus, the intensity of the main peak (feature A) was the highest for sample x = 2, decreases for x = 7 mol% Y_2O_3 and suffers a new increase for x = 12 mol% Y_2O_3. This variation of the peak intensity can be related to the different oxygen contents of the samples. The above-mentioned XANES feature (feature A) is located at about 9562 eV and corresponds to a dipole $2p \rightarrow 5d$ transition due to the empty $5d$ states and the first EXAFS oscillation. The intensity of this feature depends on the filling of the d band of hafnium ions. In this view, note that the Hf^{+4} ions ($5d^0 6s^0$) have an empty $5d$ state while the Hf^{+3} ions ($5d^0 6s^1$) are partially filled. For the sample with x = 7 mol% Y_2O_3, the peak energy and intensity of the white lines are smaller than those in the case of the samples with x = 2 and 12 mol% Y_2O_3, suggesting a smaller number of $5d$ valences.

In conclusion, the Hf XANES data do not show significant differences with increasing Y_2O_3 content of the samples suggesting an appreciable stability of the hafnium ions' +4 oxidation state and their microvicinity.

3.6. EXAFS

To verify the origin of the XANES features at the Hf edge, the spectra corresponding to the monoclinic HfO_2 structure were simulated.

The potential structural modifications and local structural changes caused to a host matrix by the addition of a dopant can be studied by EXAFS analysis and theoretical fitting procedures (Rada *et al.*, 2016). The EXAFS function was derived from the absorption data via the pre-edge and post-edge subtraction. The magnitude of the Fourier transform of EXAFS oscillations at the Hf L_3-edge of the studied ceramics

Table 1
EXAFS structural parameters for hafnium in the studied samples.

N: model coordination number of the first coordinate sphere; R: the average Hf—O interatomic distance; σ^2: parameter of Debye–Waller thermal disorder (mean squared displacement); ΔE: edge energy; ΔR: shift of bonding distance between atoms.

Sample	N	R (Å)	σ^2	ΔE (eV)	ΔR (Å)
x = 2% Y_2O_3	7	2.13041	0.00794	7.506	0.03041
x = 7% Y_2O_3	7	2.12626	0.00799	7.154	0.02626
x = 12% Y_2O_3	7	2.12059	0.00792	6.809	0.02059

is shown in Fig. 7. The EXAFS investigation detected three coordination shells around the hafnium ions for all the samples, namely Hf—O, Hf—Hf and a second Hf—Hf coordination shell at farther distances. The coordination numbers (N), average inter-atomic distances (R) and Debye–Waller disorder factors (σ^2) of the first coordination shell (Hf—O) around the hafnium ions are shown in Table 1.

The Fourier transform of the EXAFS signals at the Hf L_3-edge of all samples shows two major oscillations. The first oscillation situated in the 0.8–2.2 Å range corresponds to the nearest neighbors around the hafnium and oxygen atoms. This main peak centered at about 1.7 Å indicates the distributions of oxygen atoms around hafnium atoms and is representative of the local structure order of Hf—O bonds in the first shell. The first coordination shell is almost uninfluenced by varying the Y_2O_3 content from x = 2 to 7 mol% suggesting that the local order of Hf—O bonds is similar in both samples. After that, the increase of the Y_2O_3 content up to x = 12 mol% leads to the increase of the peak related to the Hf—O bonds suggesting an increase of the average oxidation number of hafnium (Cho *et al.*, 2017).

The coordination number and the bond length of the first Hf—O shell are 8 and 2.22 Å, respectively, for the cubic HfO_2 structure (Qi *et al.*, 2013). The EXAFS results presented in Table 1 show that in our samples the coordination numbers are around 7 and the bond lengths are ~2.12 Å that correspond to the monoclinic HfO_2 structure. The lower coordination number and the bond length are due the charge-

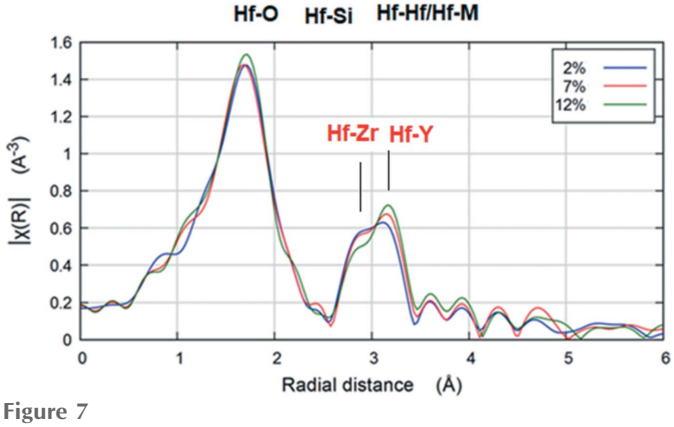

Figure 7
Magnitude of the Hf L_3-edge Fourier transform of the EXAFS oscillation for the studied samples in the $3HfO_2{\cdot}15SiO_2{\cdot}xY_2O_3{\cdot}(82-x)ZrO_2$ composition where x = 2, 7 and 12 mol% Y_2O_3.

compensating oxygen vacancies induced around the Hf atoms by addition of higher Y_2O_3 contents.

The local structural parameters presented in Table 1 show a weak compositional variation. By increasing the Y_2O_3 content of the samples the EXAFS first coordination shell distances (Hf—O distances) decrease from 2.13041 to 2.12059 Å. This evolution suggests that in sample x = 2 mol% Y_2O_3 the local environment around the hafnium ions in the first coordination shell presents a lower order in comparison with the other samples.

The second major oscillation is situated in the 2.5–3.7 Å range and is related to the next nearest neighbors such as Hf—Hf or Hf–metals paths (Sharma *et al.*, 2017). The other higher oscillations are due to the complex O–metal–O kinds of multiple scattering paths. Note that there is a significant difference in the second shell features. Thus, the fit of the second oscillation of the EXAFS signal shows that this oscillation consists of two path contributions with different lengths situated at ∼2.9 and ∼3.05 Å. The first contribution is related to the Hf—Zr (2.89 Å) and Hf—Hf (2.88 Å) bonding distances while the second contribution is associated with the Hf—Y bonding distance (3.06 Å). With increasing the yttrium content up to x = 12 mol% Y_2O_3, the last peak gradually intensifies and shifts towards higher R values. This evolution depicts an increase in the Hf–metal bond length due to the enhancement of the crystallization process of the samples.

These compositional evolutions of the EXAFS data can be regarded as an indicator of the degree of crystallization at the hafnium local environment. For the sample with x = 1 mol% Y_2O_3, the contributions from external shells are more structured in comparison with those of the samples with x = 7 and 2 mol% Y_2O_3. The differences observed for the EXAFS second coordination shell can be caused by the partial replacements of hafnium atoms by another metal atom as the second nearest neighbor of a hafnium atom, such as zirconium and yttrium atoms.

In conclusion, the EXAFS data suggest that the coordination number of the hafnium ions is around 7 and the Hf—O bond length is ∼2.12 Å, that are characteristic of the monoclinic HfO_2 structure. The contributions from the second coordination shells attributed to the Hf–metal paths become more structured by increasing the Y_2O_3 content in the host ceramic matrix.

3.7. SEM images

SEM micrographs of the samples in the $3HfO_2{\cdot}15SiO_2{\cdot}xY_2O_3{\cdot}(82-x)ZrO_2$ system with x = 2, 7 and 12 mol% Y_2O_3 are shown in Fig. 8. Due to the increase of the Y_2O_3 content, the samples x = 12 mol% will reach a more dense microstructure with smaller crystallite sizes. The high-magnification SEM image reveals that the structure of this sample consists of many domains with small and fine grains. The structural evolution of samples determined by increasing their Y_2O_3 content is in agreement with the XRD data. As was previously shown, the increase of the yttrium content determines the occurrence of yttrium–silicates precipitates (Y_2SiO_5 and $Y_2Si_2O_7$ crystalline phases) that are distributed on the surface of zirconate samples.

3.8. Raman spectroscopy

Characterization of zirconia systems by XRD may produce difficulties concerning the presence or absence of certain crystalline phases due to the highly broadened X-ray peaks.

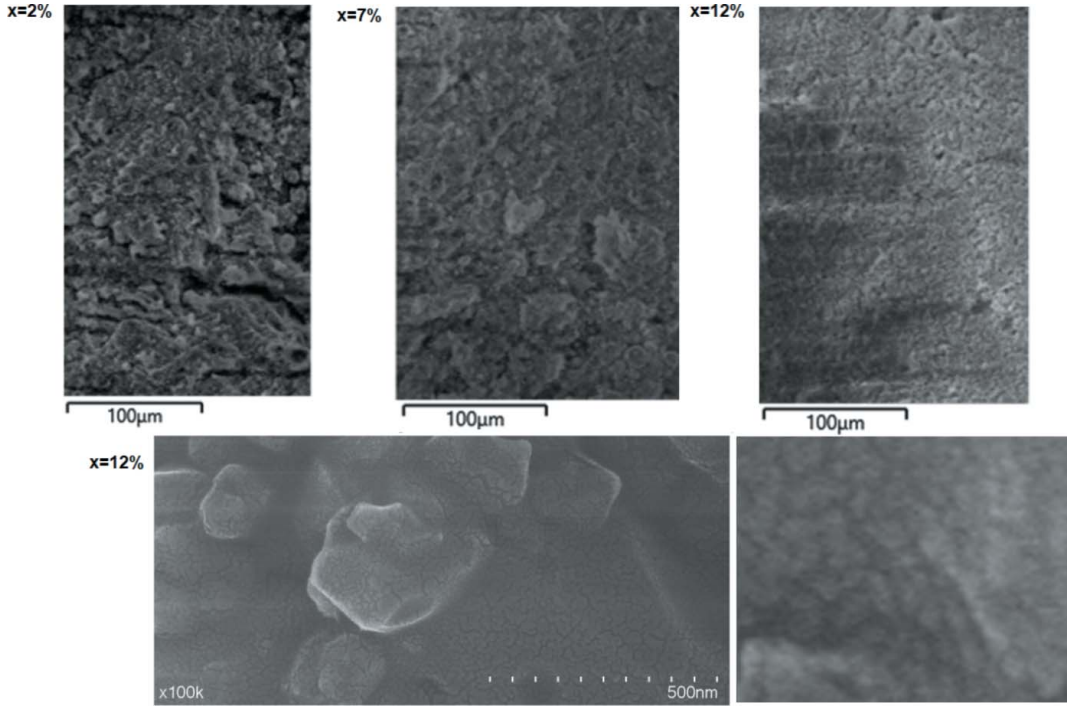

Figure 8
SEM images of the studied samples in the $3HfO_2{\cdot}15SiO_2{\cdot}xY_2O_3{\cdot}(82-x)ZrO_2$ composition with x = 2, 7 and 12 mol% Y_2O_3.

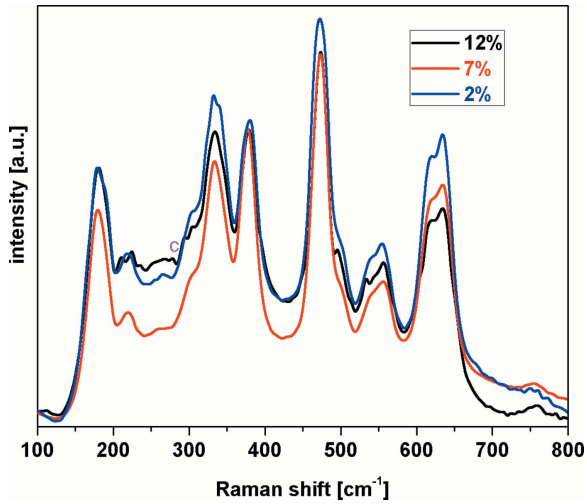

Figure 9
Raman spectra of the $3HfO_2{\cdot}15SiO_2{\cdot}xY_2O_3{\cdot}(82-x)ZrO_2$ samples with x = 2, 7 and 12 mol% Y_2O_3.

The Raman spectroscopy technique can be useful in order to help the identification of zirconia polymorphs (Ghosh *et al.*, 2006; Hartmanova *et al.*, 1998).

The Raman spectra of the $3HfO_2{\cdot}15SiO_2{\cdot}xY_2O_3{\cdot}(82-x)ZrO_2$ samples where x = 2, 7 and 12 mol% Y_2O_3 are shown in Fig. 9. The Raman bands characteristic of the monoclinic ZrO_2 phase are those located at 180, 220, 225, 300, 335, 380, 470, 535, 555, 617 and 635 cm^{-1} (Suya Prem Anand *et al.*, 2018). The tetragonal ZrO_2 phase is characterized by Raman bands centered at about 150, 255, 295, 306 and 430 cm^{-1}. Thus, the Raman spectroscopic study of the studied zirconate samples offers a clear evidence of the presence of both monoclinic and tetragonal ZrO_2 structure in the prepared samples. The intensity of the Raman band centered at about 255 cm^{-1} increases in the sample with x = 12 mol% Y_2O_3 suggesting the monoclinic → tetragonal phase transformation determined by the successive addition of Y_2O_3 to the host matrix of samples.

The complex investigations of the ceramic nanomixtures (composites) were useful tools for distinguishing the zirconia and hafnia phases and the microstructural modifications at high dopant levels. The experiments reported in this paper demonstrate the structural modifications occurring in samples by doping.

The results show that yttrium as a dopant can be successfully used in order to modify structural and behavioral properties in a desired way. The studied materials can be used for optical applications after their gap band energies are lowered below 3 eV by appropriate procedures.

In order to show the applicability of these materials in biomedicine, investigations concerning their mechanical properties and chemical stability must complete the study.

4. Conclusions

Zirconate nanostructured samples of $3HfO_2{\cdot}15SiO_2{\cdot}xY_2O_3{\cdot}(82-x)ZrO_2$ composition where x = 2, 7 and 12 mol% were prepared and studied by means of X-ray diffraction, X-ray absorption spectroscopy, SEM analysis, photoluminescence, FT-IR, Raman and UV-Vis spectroscopy. XRD and XAS techniques were used to identify the crystalline phases from the studied samples. Thus, the presence of the following crystalline phases was observed: t-ZrO_2, m-ZrO_2, m-HfO_2, Y_2SiO_5 and Y_2SiO_5. SEM investigation highlighted the presence of Y_2SiO_5 and $Y_2Si_2O_7$ crystalline phases, in agreement with XRD data.

The photoluminescence emission bands are associated with structural defects such as the oxygen vacancies in monoclinic ZrO_2 and monoclinic HfO_2 structures. Based on the UV-Vis spectroscopy data, the gap energy of the samples was determined. The compositional evolution of gap energy values shows that the increase of the xY_2O_3 content of the samples led to the enhancement of the crystallization process in agreement with the XRD data. Smaller values of the gap energy can also be related to smaller average crystallite sizes, in agreement with the SEM data.

FT-IR and Raman spectroscopies were useful tools for distinguishing the zirconia phases. Thus, it was observed that the increase of the Y_2O_3 content of samples led to an increase of the t-ZrO_2 and silicate crystalline phases. The structural changes observed by the FT-IR and Raman investigations suggest that the yttrium ions play a network modifier role in the studied system.

The local structure around the Hf cations from the studied ceramic nanomixtures was studied by analysing the Hf L_3-edge EXAFS spectra obtained at room temperature. The EXAFS analysis suggests smaller deviations in bond length sets of Hf—O shells with increasing Y_2O_3 content in the host ceramic matrix. The contributions from the second coordination shells attributed to the Hf–metal paths are more structured by increasing the Y_2O_3 content in studied ceramics.

Acknowledgements

This work was supported by the grants PN-III-P2-2.1: 77BG/2016 and 246MC/2017. SEM and Raman investigations were performed at INCDTIM.

References

Balaji, S., Mandal, B. K., Ranjan, S., Dasgupta, N. & Chidambaram, R. (2017). *J. Photochem. Photobiol. B*, **170**, 125–133.
Benyagoub, A. (2012). *Acta Mater.* **60**, 5662–5669.
Cho, D., Luebben, M., Wiefels, S., Lee, K. & Valov, I. (2017). *Appl. Mater. Interfaces*, **9**, 19287–19295.
Choi, D. & Choy, K. (2016). *Electrochim. Acta*, **218**, 47–53.
Chu, H., Hwang, W., Du, J., Chen, K. & Wang, M. (2016). *J. Alloys Compd.* **678**, 518–526.
Chuang, S., Lin, H. & Chen, C. (2012). *J. Alloys Compd.* **534**, 42–46.
Dehelean, A., Rada, S., Popa, A., Suciu, R. C. & Culea, E. (2016). *J. Lumin.* **177**, 65–70.
Fan, Y., Cheng, S., Wang, H., Tian, J., Xie, S., Pei, Y., Qiao, M. & Zong, B. (2017). *Appl. Catal. Environ.* **217**, 331–341.
Ferdov, S., Ferreira, R. A. S., Lin, Z. & Wu, Z. (2012). *J. Solid State Chem.* **190**, 18–23.
Ghosh, A., Suri, A. K., Pandey, M., Thomas, S., Rama Mohan, T. R. & Rao, B. T. (2006). *Mater. Lett.* **60**, 1170–1173.
Glazneva, T. S., Kaichev, V. V., Paukshtis, E. A., Khabibulin, D. F., Lapina, O. B., Bal'zhinimaev, B. S., Zhurba, E. N., Lavrinovich, I. A.,

Gavrikova, I. N., Shumskii, V. I. & Trofimov, A. N. (2012). *J. Non-Cryst. Solids*, **358**, 1053–1058.
Hartmanova, I., Thurzo, M., Jergel, I., Bartos, F., Kadlec, V., Zelezny, D., Tunega, F., Kundracik, F., Chromik, S. & Brunel, M. (1998). *J. Mater. Sci.* **33**, 969–975.
Karunarathne, M. C., Baumann, J. W., Heeg, M. J., Martin, P. D. & Winter, C. H. (2017). *J. Organomet. Chem.* **847**, 204–212.
Khomenkova, L., An, Y., Khomenkov, D., Portier, X., Labbé, C. & Gourbilleau, F. (2014). *Physica B*, **453**, 100–106.
Kiisk, V., Puust, L., Utt, K., Maaroos, A., Mändar, H., Viviani, E., Piccinelli, F., Saar, R., Joost, U. & Sildos, I. (2016). *J. Lumin.* **174**, 49–55.
Kwon, O. H., Jang, C., Lee, J., Jeong, H. Y., Kwon, Y., Joo, J. H. & Kim, H. (2017). *Ceram. Int.* **43**, 8236–8245.
Lee, S. W. & Condrate, R. A. (1988). *J. Mater. Sci.* **23**, 2951–2959.
Moll, S., Thomé, L., Sattonnay, G., Garrido, F., Vincent, L., Jagielski, J. & Thomé, T. (2009). *Vacuum*, **83**, S61–S64.
Najafinezhad, A., Abdellahi, M., Ghayour, H., Soheily, A., Chami, A. & Khandan, A. (2017). *Mater. Sci. Eng. C*, **72**, 259–267.
Ortiz, A., Alonso, J. C. & Haro-Poniatowski, E. (2005). *J. Elec Mater.* **34**, 150–155.
Ponnilavan, V., Vasanthavel, S., Singh, R. K. & Kannan, S. (2015). *Ceram. Int.* **41**, 7632–7639.
Qi, J. & Zhou, X. (2015). *Colloids Surf. A Physicochem. Eng. Asp.* **487**, 26–34.
Qi, Z., Cheng, X., Zhang, G., Li, T., Wang, Y., Shao, T., Li, C. & He, B. (2013). *Mater. Res. Bull.* **48**, 2720–2723.
Qin, H., Liu, H., Sang, Y., Lv, Y., Zhang, X., Zhang, Y., Ohachi, T. & Wang, J. (2012). *CrystEngComm*, **14**, 1783–1789.
Rada, M., Aldea, N., Wu, Z. H., Jing, Z., Rada, S., Culea, E., Macavei, S., Balan, R., Suciu, R. C., Erhan, R. V. & Bodnarchuk, V. (2016). *Journal of Non-Crystalline Solids*, **437**, 10–16.
Rada, M., Zagrai, M., Rada, S., Bot, A. & Culea, E. (2017). *J. Alloys Compd.* **705**, 327–332.
Rada, M., Zhang, J., Zhongua, W., Zagrai, M., Magerusan, L. & Rada, S. (2018). *Anal. Lett.* **51**, 2544–2550.
Rada, S., Culea, E. & Rada, M. (2018). *Chem. Phys. Lett.* **696**, 92–99.
Rada, S., Rada, M. & Culea, E. (2013). *J. Alloys Compd.* **552**, 10–13.
Rada, S., Rada, M., Erhan, R. V., Bodnarchuk, V., Barbu-Tudoran, L. & Culea, E. (2019). *J. Alloys Compd.* **770**, 395–404.
Sharma, A., Varshney, M., Shin, H., Chae, K. & Won, S. O. (2017). *Spectrochim. Acta A Mol. Biomol. Spectrosc.* **173**, 549–555.
Simhan, R. G. (1983). *J. Non-Cryst. Solids*, **54**, 335–343.
Singh, S., Kalia, G. & Singh, K. (2015). *J. Mol. Struct.* **1086**, 239–245.
Suya Prem Anand, P., Arunachalam, N. & Vijayaraghavan, L. (2018). *J. Mech. Behav. Biomed. Mater.* **86**, 122–130.
Torres, D. I. & Llopis, J. (2009). *Superlattice Microstruct.* **45**, 482–488.
Villabona-Leal, E. G., Diaz-Torres, L. A., Desirena, H., Rodríguez-López, J. L., Pérez, E. & Meza, O. (2014). *J. Lumin.* **146**, 398–403.
Vitanov, P., Harizanova, A. & Ivanova, T. (2014). *J. Phys. Conf. Ser.* **514**, 012011.
Wu, L., Wu, C. G. & Chang, Y. (1992). *J. Electron. Mater.* **21**, 217–222.
Zhen, Q., Chen, R., Van, K. & Li, R. (2007). *J. Rare Earths*, **25**, 199–203.